The optimal electrode hole size in zero gap alkaline water electrolysis
A combined electrochemical, theoretical, and bubble imaging approach

Haverkort, J. W.; Aghdam, A. S.; Craye, E.

DOI
10.1016/j.ijhydene.2025.150919

Publication date
2025

Document Version
Final published version

Published in
International Journal of Hydrogen Energy

International Journal of Hydrogen Energy 171 (2025) 150919

Contents lists available at ScienceDirect

International Journal of Hydrogen Energy

journal homepage: www.elsevier.com/locate/he

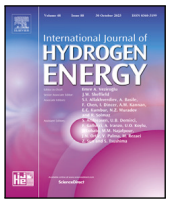

The optimal electrode hole size in zero gap alkaline water electrolysis: A combined electrochemical, theoretical, and bubble imaging approach

J.W. Haverkort *, A.S. Aghdam, E.J.B. Craye

Delft University of Technology, Process & Energy Department, Leeghwaterstraat 39, Delft, 2628 CB, The Netherlands

ARTICLE INFO

Keywords:
Alkaline water electrolysis
Zero-gap electrodes
Gas evolution
Hydrogen bubbles
Electrode shape

ABSTRACT

The ohmic resistance of an alkaline water electrolyser for green hydrogen production can be reduced by minimising the distance between the electrodes and the diaphragm. A zero-gap configuration requires holes in the electrode to transport the produced gases to the backside of the electrode. Industry typically uses expanded metals and perforated plates with hole sizes of one or a few millimetres, but the optimal hole size is not known. In this study, we experimentally assess the overpotentials as a function of hole size, shape, and open area fraction using a wide variety of electroformed nickel electrodes of 30 cm^2 up to 10^4 A/m^2 in 80 °C 30 w% KOH. We find that for sub-millimetre holes, the overpotentials strongly increase as hole size decreases. The reason is that small hole sizes make it difficult for the gas bubbles to leave effectively, leading to coalescence and clogging. Consequently, a gas film can arise between the electrode and the diaphragm, as shown by through-the-membrane images. Therefore, the increased surface area associated with these small holes is not effectively used. We show that performance can be improved by taking away surface area through additional larger holes in a small hole-size electrode, which allow bubbles to effectively evacuate from the electrodes.

1. Introduction

Alkaline water electrolysis is presently the most proven and cost-effective type of water electrolysis to produce green hydrogen [1]. In a zero-gap configuration, to reduce the resistance, a perforated electrode is positioned directly onto the diaphragm that separates the produced hydrogen and oxygen. A wealth of literature exists on the influence of the type of catalyst on overpotentials of the hydrogen and oxygen evolution reactions [2], as well as the influence of the electrode surface roughness [3,4] or tailored microstructure [5–12]. A combination of nickel and iron was found to be an affordable and efficient electrode material for both the anode and the cathode [13]. Much less studied is the influence of the electrode shape, or 'form factor', on alkaline water electrolysis. Some studies exist on wire meshes [3,14–16], expanded metals [17–20], porous metal foams [21,22], and 3D-printed electrodes [23,24]. In a recent work [25], the oxygen evolution reaction overpotential at $8 \cdot 10^3$ A/m^2 was found to be minimised by an electrode thickness of around 0.5 mm, obtained by stacking 3–5 meshes with apertures of 0.2 mm. Presumably, bubble accumulation causes larger overpotentials in thicker electrodes. Interestingly, meshes with smaller apertures can be made much thicker without showing this deleterious effect.

Here, we are concerned only with single layers of perforated plate-type electrodes in zero gap. Very few studies mention the requirements for hole dimensions in such electrodes. Smaller holes can increase the electrode surface area and decrease the activation overpotentials, but also make it harder for bubbles to escape. Too large holes can lead to a more inhomogeneous current distribution, increasing the resistance. Therefore, an optimal hole size may exist. Kienzlen et al. [26] compared various perforated electrodes and found no pronounced optimal hole size but did notice that for their smallest used hole size of 60 μm, an obstructing gas film forms that is not there for their second smallest hole size of 300 μm. They conclude that the hole size should be at least around 200 μm to allow bubbles to leave effectively. The data from Ref. [27] is not so clearly presented, but an optimal opening between 0.1–0.3 mm is mentioned for the cathode, while it is suggested that anode holes should be larger than 1.2 mm at 10^4 A/m^2. For solid foams, Ref. [22] recommends using a thickness of 1 mm and a pore size of around 0.3 mm for the hydrogen evolution reaction. Thicker electrodes are argued to increase bubble resistance. Ref. [28] tested three nickel foams, a mesh and a perforated plate and found the best performance for foams with a hole size of 0.43 mm at the anode and 0.23 mm at the cathode. This strongly contrasts with the results of Ref. [29], where a high bubble resistance of 1.8 Ω cm^2 was found for 0.4 mm pore size in 1M KOH, versus 0.3 Ω cm^2 for plates perforated with 1 mm diameter holes. Ref. [14] tested eight different woven meshes and five expanded metals and found that a lower ratio of pore size

* Corresponding author.
E-mail address: J.W.Haverkort@tudelft.nl (J.W. Haverkort).

https://doi.org/10.1016/j.ijhydene.2025.150919
Received 4 June 2025; Received in revised form 21 July 2025; Accepted 9 August 2025
Available online 3 September 2025

to wire thickness reduced the overpotential. Ref. [30] studied various expanded metals, meshes, and perforated plate electrodes, as well as different diaphragms, showing that both strongly influence the bubble behaviour.

Several papers mention expected benefits from electrode shapes that divert gas away from the diaphragm [31,32]. In the context of chlor-alkali electrolysis, Ref. [17] finds that unflattened expanded metal electrodes perform better as cathodes than flattened versions, presumably due to their improved capacity for gas removal towards the back of the electrode. Two-dimensional computational 'primary current distribution' simulations predicted a linear decrease in cell voltage with decreasing hole size and open area fraction [33]. It was mentioned that likely an optimum hole size exists, as too small holes will lead to gas accumulation [33]. In a real chlor-alkali cell, the simulation results were found to approximately hold for louvred electrodes but only weakly for perforated plates and flattened mesh anodes [34]. Below an open area fraction of 30%, pronounced bubble accumulation was observed, so 40% was recommended. Ref. [35] also stressed that to ensure a homogeneous current distribution, the distance between perforations should be kept as small as possible but not so small that gas removal is impeded. The anomalously large resistance observed in various zero-gap alkaline electrolysers [36] was argued to be due to inhomogeneous current distributions aggravated by gas formation in the small gap between the electrode and the diaphragm. The side of the electrode facing the diaphragm was even observed to become effectively inactive, likely due to gas formation [20]. In Ref. [37], electrodes similar to those used in this work were studied but etched and cleaned to improve wettability at room temperature up to $4 \cdot 10^3$ A/m^2. Bubbles were found to block the smaller holes electrode protrusions were hypothesised to have a positive effect on bubble removal.

Recently, several papers measured the overpotentials of bubbles on or near nickel electrode, using electrochemical impedance spectroscopy (EIS) [38–40]. Depending on the smoothness of the surface, Ref. [38] found an additional areal resistance of $1 - 2 \cdot 10^{-3}$ Ω cm^2 times the square root of the current density in A/m^2, on a 5 mm diameter vertical cylindrical nickel rod in 1 M KOH at room temperature. Ref. [39] finds a similar sublinear increase in resistance with current density using 150–300 μm diameter horizontal cylindrical nickel wire electrodes in 2 M KOH at 30 °C, but about an order smaller in magnitude. Besides the higher conductivity, the smallness of the electrode may have helped in bubble removal. The dynamic viscosity of the electrolyte increases with increasing concentration and decreasing temperature [41], which may also impact the results.

The resistance contribution was roughly twice as large for the anode compared to the cathode. Under similar conditions, Ref. [40] finds for planar vertical nickel electrodes an additional cell overpotential of 0.2 V at $6 \cdot 10^3$ A/m^2, with a resistance that increases with increasing current density.

Here, we provide a large measurement dataset using 18 different electrodes with hole sizes varying between 37 μm and 8 mm. Various shapes of holes and protrusions, including circular, square, and star-shaped holes, are used. Open area fractions vary between 7%–51%, and the electrode thickness varies between 0.255–1.4 mm. This wide variety allows us to find out what electrode features are most important. Our use of reference electrodes and video imaging aids understanding of the data. The relatively large electrode area, high temperature, current density, and electrolyte concentration make our results directly relevant to industrial practice.

2. Methods

2.1. Electrodes

Table SI-1 in the supporting information file shows the used electrodes. The fourteen electrodes labelled ZP were supplied by Veco Precision B.V. and were produced by electroforming, resulting in pure nickel. Similar electrodes were used in Refs. [37,42–44]. Various hole shapes were fabricated, and due to the fabrication method, besides a flat 'shiny' side, these electrodes show varying degrees of protrusions or pillar thicknesses on top of their base thickness. The hole areas ranged between $3.3 \cdot 10^{-3} - 2.0$ mm^2, the open area fraction between 6.7% and 46%, base thicknesses between 255 and 538 μm, and pillar heights between 0 μm and 880 μm. The dimensions in Table SI-1 were obtained by analysing scanning electron microscopy images of the flat side using a JEOL JSM-6500F. The specific electrical resistance was obtained using a four-electrode measurement on 17.5 cm long, 1 cm wide strips. The average of ten ±50 mV potential scans, performed at a scan rate of 1 mV/s using a Gamry Reference 3000 potentiostat, was used. The four electrodes named x mm contain square holes of x by x millimetre. The holes were cut in a 99.9% pure nickel plate purchased from Evek GmbH using a water jet. Their open area fractions range from 48% to 51.2%.

A Lion Alpha laser jet cutter was used to make L-shaped electrodes with an active area of 30 cm^2, measuring 4 cm in width and 7.5 cm in height with, with a 0.8 cm wide, 3.5 cm long stem in the top corner to facilitate secure fastening of the potentiostat leads. Each electrode was prepared in twofold for use as an anode and as cathode. These relatively large electrode dimensions allow minimising edge effects and ensure industrially relevant turbulent flow conditions over a significant part of the electrode area. The high electronic conductivity of nickel allows for a maximum potential drop over the electrode of roughly 10 mV, and hence a good current homogeneity. After cleaning the electrodes with an acetone ultrasonic bath for ten minutes, they were rinsed with Milli-Q water (18.2 MΩ cm at 25 °C) and put in an ultrasonic bath for another ten minutes.

The hydraulic diameters were obtained by dividing four times the area of the hole by its perimeter. For circular holes, this measure equals the diameter, for square holes the side length, while for more elongated shapes it tends to twice the smallest dimension. The hydraulic diameter has the advantage that it can be straightforwardly defined and calculated for any shape. It is often used in turbulent channel flow, where pressure drops scale with the channel wall area. Also, in Taylor flow, where large bubbles leave only a thin liquid layer near the wall, the wetted perimeter and hydraulic diameter are often an effective metric. [45,46]. However, other measures effectively characterising the hole size may similarly be used.

2.2. Cell design

To achieve a zero-gap configuration, the anode and cathode were mounted on a membrane using five nylon bolts as shown in Fig. 1(left). The holes for these bolt were positioned relative to the edges of the electrodes equally for all electrodes. The used 0.5 mm thick Zirfon PERL UTP 500 diaphragm by Agfa is an industrially used porous material made from PSU-reinforced ZrO_2 with a porosity of 50% and an average pore size of 0.15 μm. The electrochemical cell shown in Fig. 1 was 3D-printed with a stereolithography (SLA) Form 3B+ printer (Formlabs) using Clear Resin V4 to KOH and impermeable to water. The two front plates of the electrochemical cell were made using stainless steel 316 to improve the heat conduction to and from the cell. A lid covering the cell was added to prevent as much as electrolyte leaving through evaporation and as mist droplets. A 30% w/w potassium hydroxide electrolyte was made from purified water (18.2 MΩ cm at 25 °C) and ACS reagent pellets KOH pellets, whose ≥ 85% purity was taken into account in calculating the concentration. An electrolyte volume of 2.5 × 5.5 × 8.5 = 116.9 cm^3 on both the cathode and anode side was used, giving 223.8 cm^3 in total.

The cell was heated up and cooled down using a one-litre water bath equipped with a copper coil. The temperature of the water in the copper coil was adjusted using a Lauda RC6-CP in a feedback loop with the PT-100 temperature sensor in the electrolyte bath.

The booster cables are bolted onto the anode and cathode as shown in Fig. 1(right), and four additional voltages, those of the anode, cathode, anolyte reference electrode and catholyte reference electrode, were logged with a NI-6002 DAQ.

Fig. 1. Top: The L-shaped electrodes were compressed with five nylon bolts onto the diaphragm to approach a zero-gap configuration. Bottom left: The 3D-printed beaker cell with stainless steel end plates, electrodes, and holes for the reference electrodes and temperature probe. Bottom right: The cell was submerged in a heating bath with a coil that can both heat and cool. The booster cables were bolted onto the anode and cathode, and various cables for voltage measurement are shown. The blueish taint on the right, compared to the more yellow colour on the left picture, comes with heating and wetting.

2.3. Voltage measurements

A Gamry Reference 3000 potentiostat with 30 A booster was used for all experiments. The applied current was swept from 30 A (10^4 A/m^2) down to 0.0179 A (5.97 A/m^2) with 65 steps in a logarithmic scale and back up to 30 A (10^4 A/m^2) with another 65 steps. The electrodes were preconditioned at 10^4 A/m^2 for 600 s, followed by a current sweep in which each current was maintained for 30 s. Refs. [20, 47] found that over this time scale hydrodynamic effects have largely stabilised. The time-averaged voltage over the last 5 s is reported here.

In a preliminary once-off experiment, ambient conditions were used without controlling the electrolyte temperature. Most electrodes were tested twice, first with pillars towards the diaphragm and next away from the diaphragm (See s).

In the main experiments, the temperature of the electrolyte was fixed at 80 °C using the heating and cooling bath. The same electrodes that were used in the preliminary experiments were used, supplemented with our own square-hole samples. The current sweep was the same as in the preliminary experiments; however, the preconditioning time with 10^4 A/m^2 was extended to 1800 s to more or less stabilise the kinetic properties of Nickel.

Each electrode in Table SI-1 was tested three times, spread out over several weeks. Only the second and third time reference electrodes were used. Two Hg/HgO reference electrodes with 6 mm diameter (EF-1369 by BASi®) were filled with 1 M NaOH solution. They were immersed in the bulk electrolyte on separate sides, one in the anolyte and one in the catholyte. Unfortunately, we found that data from these reference electrodes occasionally demonstrated unexpected behaviour, particularly in run 3. Therefore, we used the data from run 2 to determine the electrolyte potential drop between the anolyte and catholyte reference electrodes, except for the electrodes with d_h = 602 μm (ZP200000), 2 mm, and 4 mm, for which the run 3 data was more reliable. In reporting the electrolyte potential drop we subtracted a small calibration offset for zero current density, obtained from a least squares fit.

In reporting the activation overpotentials we entirely excluded the cathode data for d_h = 37 and 602 μm in run 2 and d_h = 224 and 353 μm, 2 mm, and 8 mm in run 3, and the anode data of 50 μm in run 2 and d_h = 224, 292, 353 μm, 2 mm and 8 mm in run 3. Therefore, these data points consist only of a single measurement. In the third run, ZP200721 (d_h = 353 μm) was not included, so the reference electrode data for this sample comes only from the second run. The electrode ZP200687 with d_h = 393 μm, the 2 mm and the 8 mm were excluded since in both runs the reference electrodes gave erroneous values data.

Note that the obtained cell voltages in this work are very high compared to those obtained in optimised systems in the literature or in industrial electrolysers. The primary reason is our use of pristine nickel. Especially at the cathode and without much uptake of iron from the solution, nickel is far from an optimal catalyst material and incurs large overpotentials. We symmetrically use nickel here for reasons of manufacturability, and since we primarily study the differences between the various electrodes, this high overall cell voltage should not bother us too much. The relatively strong performance variation in time of both the catalytic properties of nickel [48], as well as the integrity of the zero gap [49] are more of a concern for reproducibility that can only be partially taken away by our use of systematic procedures and repeat experiments.

We found a significant hysteresis between the voltages recorded during the decreasing part of the current sweep compared to the increasing part. Especially at low current densities, the latter were significantly lower on average. An interesting exception was ZP100890 (d_h = 1.6 mm), which showed an almost 15% lower voltage at 10^4 A/m^2 during the upsweep of run 1 compared to the downsweep.

For most electrodes, somewhere during the downsweep below 10^2 A/m^2 a relatively rapid transition to lower voltages was observed. Likely, this is at least in part due to oxidation reactions at the anode, although the presence of gas remaining in potential space between the diaphragm and electrode could also play some role. Therefore, we will only use the data from the downwards current sweep between 10^2 and 10^4 A/m^2 and focus primarily on the highest current densities.

We note that the voltage measured by the potentiostat sometimes fluctuated significantly, sometimes wildly, especially in the 10^3 – 10^4 A/m^2 range. Ref. [47] finds similar but more regular fluctuations to be due to gas slugs in the electrode-diaphragm gap.

2.4. Imaging

Next to the electrochemical measurements, the electrodes were imaged in operando, such that the bubble behaviour around the different electrode geometries could be better understood. For this, a Photron FASTCAM Nova S12 high-speed camera was used. This allowed imaging at 1000 fps at a resolution of 1024 x 1024. A Laowa 25 mm F/2.8 2.5-5X Ultra-Macro lens was used in combination with this camera, which allowed magnification of up to 5X. A Photron FASTCAM Viewer 4 was used to control the camera.

To image the bubble behaviour near the electrode geometries, two different cell configurations were used. A top-view schematic of both can be found in Fig. 2. For normal back-side viewing, the electrodes were bolted to the Zirfon diaphragm, and the assembly was submerged in a PMMA beaker containing a 6M KOH solution. Imaging was performed through the PMMA directly onto the electrode. For the more challenging front-side imaging, a modified setup is used. The counter electrode was placed further away, and contained a 6 mm slit, such that imaging could be done through this electrode with minimal impact on current homogeneity. The electrode was surrounded by a diaphragm, such that evolved bubbles do not hinder the view on the working

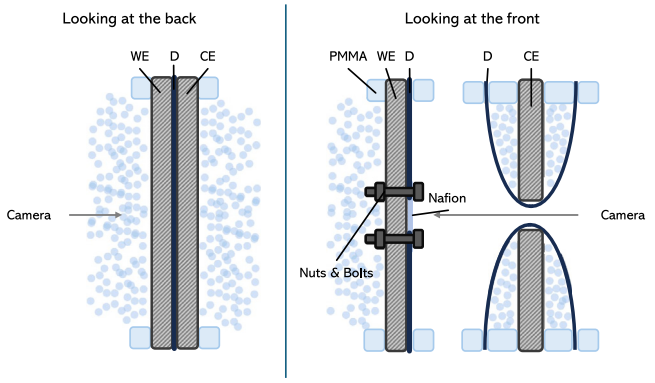

Fig. 2. Left: top-view schematic of the working electrode (WE) of interest, counter electrode (CE) and diaphragm (D) used to image electrodes from the back (electrolyte side). Right: top-view schematic of the setup used to image electrode from the front (membrane side). A 3 × 3 mm hole is cut in the diaphragm, where the transparent Nafion takes over. The counter electrode contains a 6 mm slit to allow camera viewing, along the direction of the grey arrow, and is surrounded by a diaphragm to avoid bubbles in the way.

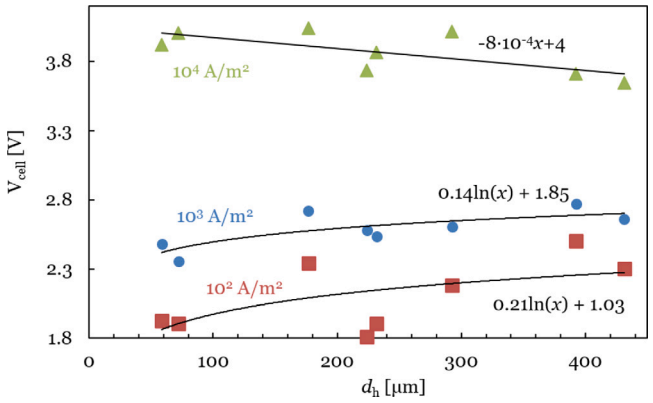

Fig. 3. Preliminary non-temperature-controlled room-temperature measurements with electrode pillars oriented towards the diaphragm, tentatively showing the cell voltage, V_{cell}, decreases a function of the hydraulic diameter of the holes, d_h, for a current density of 10^4 A/m^2 but increases for 10^3 and 10^2 A/m^2. The latter may be explained by the higher surface area of smaller holes and pillars. The shown lines are primarily a guide to the eye. The very rough logarithmic fits, with a slope in the order of the combined anodic and cathodic Tafel slope, may be an indication of decreasing activation losses due to increasing surface area as the hydraulic hole diameter decreases. The decreasing trend with increasing d_h, for $j = 10^4$ A/m^2, is attributed to additional bubble resistance, which will be discussed in more detail in subsequent sections.

electrode. In addition to the Zirfon UTP 500 membrane, a Nafion 117 membrane was locally bolted onto the working electrode. This resulted in a 3 by 3 mm window offering a look on the front side of the electrode. The inter-electrode distance between the working and counter-electrode was 1.7 cm. This assembly was then submerged in a PMMA beaker containing a 6M KOH solution. To justify the use of the Nafion membrane as a reasonable substitute for the opaque Zirfon, a contact angle experiment was performed on both the Nafion membrane and the Zirfon UTP 500 diaphragm. Using 34 bubbles, the average wetting angle of hydrogen bubbles in a 6M KOH solution on a Nafion membrane was $43.2 \pm 2.4°$, while on a Zirfon UTP 500 diaphragm this angle was $39.1 \pm 3.1°$ [47].

3. Results

3.1. Pillars towards or away from the diaphragm?

Many of the electrodes tested have protrusions, or pillars, extending beyond the base plane of the electrode, see Table SI-1. A first obvious question to investigate is whether these protrusions should be oriented away from or toward the diaphragm. Ref. [37] found that pillars can damage the diaphragm, causing short-circuiting. This did not happen in our tests, and Fig. 3 shows the measured cell voltages. In this graph and most other graphs below, we plot our data as a function of the hydraulic diameter of the holes, as determined from images of the flat side. In these preliminary tests, we did not control for temperature and heat production in the reaction likely caused the temperature to be somewhat elevated over room temperature.

It can be seen that while for high current densities the smallest holes have the highest cell voltage, this trend is reversed for the lower current densities, where the smallest holes perform best. A plausible explanation is that for larger current densities, gas fraction effects dominate and increase the resistance. For lower current densities, less gas is generated. Additionally, activation overpotentials that scale logarithmically in the current density are, at low current densities, relatively more important than ohmic losses, which scale linearly. The surface area of the holes and pillars scale roughly inversely proportional to the hydraulic diameter of the holes, providing an explanation for why the electrodes with the smallest holes have the lowest cell voltage for the lowest current densities in Fig. 3.

We did not control the temperature and did not do repeat experiments with pillars oriented towards the diaphragm, so we do not show the data of these preliminary experiments here. They did provide a clear picture and showed that with the pillars towards the diaphragm, the cell voltage at 10^4 A/m^2 was, on average, about 12% increased compared to with the pillars oriented away from the diaphragm. At 10^3 A/m^2 and 10^2 A/m^2 the increases were, with 4% and 1% respectively, smaller but consistently there for virtually all electrodes. Therefore, in the rest of this work, we focus on the configuration with the pillars away from the diaphragm.

3.2. Hole size

The cell voltages recorded during three independent measurements were averaged and analysed for their dependence on hole dimensions, open-area fraction, base thickness, pillar thickness, and electrode resistance. The clearest trend was observed as a function of the hydraulic hole diameter, as shown in Fig. 4 for 10^4 A/m^2. For most of the tested electrodes, the smaller the hole size, the smaller the open area fraction. Also, most, but not all, electrodes with small holes had relatively large pillar sizes. Therefore, these parameters also showed a significant correlation with the cell voltage. However, after correcting for the trend with hydraulic diameter, no dependence on these parameters remained.

It is clear from Fig. 4 that the smallest holes give the largest cell voltage. To model this, we propose to split off terms that depend on the hydraulic diameter. We first consider terms that do not depend on hole size, due to the diaphragm resistance R, the equilibrium voltage $V_{eq} = 1.23$ V for water splitting, and activation losses. In the Tafel regime, we can write [51]:

$$V_0(j) = \overbrace{V_{\mathrm{eq}}}^{\text{equilibrium}} + \overbrace{ARj}^{\text{ohmic}} + \overbrace{b \ln\left(j/J_* \mathcal{E}\right)}^{\text{activation}} \tag{1}$$

where b and J_* are the effective combined anodic and cathodic Tafel slope and exchange current density. To this, we add two ad-hoc terms that respectively decreases and increase with increasing hydraulic diameter of the holes d_h, to give the cell voltage as

$$V_{\mathrm{cell}} = \overbrace{V_0(j)}^{\text{Eq. (1)}} + \overbrace{\frac{\Delta V(j)}{1 + d_h/d_c}}^{\text{bubble transport, } \eta_{tr}} + \overbrace{f\frac{j d_h}{\kappa_0}}^{\text{current distribution}} \tag{2}$$

The solid line in Fig. 4 shows this function for $f \approx 0.6$ and $d_c = 0.5$ mm and $\Delta V = 0.9$ V, which were fitted to the data. The second term in Eq. (2), which we somewhat ambiguously refer to as a transport

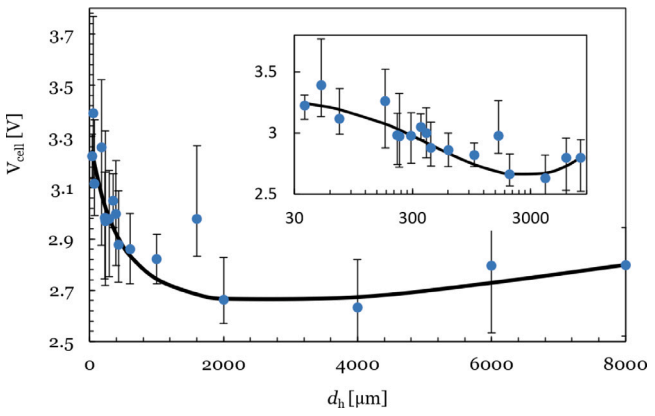

Fig. 4. The measured cell voltage V_{cell} at a current density $j = 10^4$ A/m^2 in 80 °C, 30 w% KOH, for the various electroformed ($d_h < 2$ mm) and perforated plate ($d_h > 2$ mm) nickel electrodes of Table SI-1 as a function of hydraulic diameter d_h of their holes. The average, minimum, and maximum over three runs are indicated by the circles, lower, and higher error bars, respectively. The line give Eqs. (2) and Eq. (1) with: $V_0 = 2.4$ V, $\Delta V = 0.9$ V, $d_c = 0.5$ mm, $\kappa_0 = 139$ S/m [50] and $f = 0.6$ so $f j d_c/\kappa_0 \approx 0.02$ V. The inset graph shows the same in a Tafel plot with the current density on a logarithmic scale.

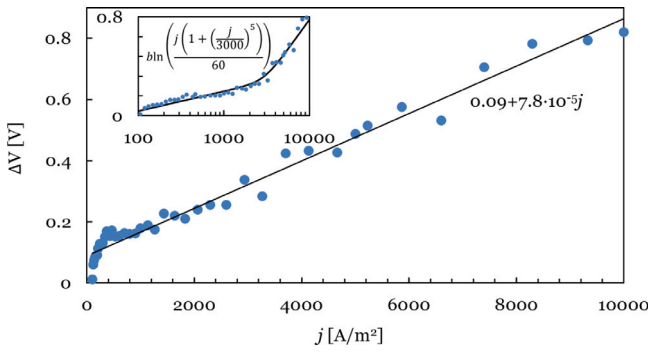

Fig. 5. The value of ΔV determining the transport losses $\frac{\Delta V(j)}{1+d_h/d_c}$ due to too small holes in Eq. (2), as a function of the current density j [A/m^2] on a logarithmic scale. It is obtained from fitting the cell potential minus the last term of Eq. (2) as a function of $\frac{1}{1+d_h/d_c}$, using $d_c = 0.5$ mm. The data averaged over the second and third run was used, and we excluded the outlier in Fig. 4 with $d_h = 1.6$ mm from the fit. An offset-linear fit describes ΔV reasonably well at higher current densities. The inset shows that at low current densities, a logarithmic dependency with Tafel slope $b = 0.07$ V (≈ 160 mV/decade) can also provide a reasonable representation. At high current densities, this slope increases about 6-fold.

overpotential, is a simple fitting function to take into account the increase in cell voltage observed for smaller hole sizes. For hole sizes $d_h \ll$, it tends to ΔV, for $d_h = d_c$ it becomes $\Delta V/2$, and for $d_h \gg d_h$ it tends to zero. The final term is the additional ohmic drop over a distance $f d_h$, proportional to unobstructed electrolyte conductivity κ_0.

The effective electrolyte conductivity

$$\kappa = \epsilon(1-\varepsilon_g)^{3/2}\kappa_0 \tag{3}$$

is reduced compared to the solution value κ_0 with the open-area fraction ϵ, and the gas fraction ε_g. The power 3/2 approximately takes into account the effect of the bubbles on the tortuosity through Bruggeman's relation [51,52].

A term similar to the final term in Eq. (2) was also found in the two-dimensional simulations of Ref. [53] assuming Butler–Volmer kinetics. It was shown to be due to the inhomogeneity in the current distribution introduced by larger hole sizes. In our notation, and using Eq. (3), the result of the simulations of Ref. [53] can be written as $f = 0.18\epsilon^{2.1}(\kappa_m/\kappa)$. Our fitted value $f = 0.6$ requires, with $\epsilon = 0.5$ for the largest hole size electrode, a gas fraction $\varepsilon_g \approx 0.82$ to be in agreement with this simulation result. This value is above the maximum packing fraction of equal diameter spheres of 0.74 and the maximum gas fraction used in Ref. [54]. Therefore, these current distribution simulations, while of the right order of magnitude and trend, underestimate these losses. One reason may be that in these simulations the front of the electrode was assumed to be fully available for the reaction, which may not always be the case in a zero-gap electrode configuration [20]. In our experiments and in these simulations, the holes were almost perfectly aligned with similar-sized holes on the opposing electrode. In practice, this will not generally be the case, and in 1, we provide a simple model for what could be an additional resistance as a consequence.

With $\Delta V = 0.9$ V, the second term in Eq. (2) is very large at 10^4 A/m^2. Let us next investigate its dependence on current density. We subtracted from the average measured cell voltage the final term of Eq. (2) and made an offset-linear least squares fit versus $\frac{1}{d_h/d_c}$, the slope of which is ΔV. We excluded electrode ZP100890 with hole diameter $d_h \leq 1.6$ mm, which for an unknown reason did not respect the trend observed in the other electrodes.

The result shown in Fig. 5 shows that ΔV increases more or less linearly in the current density but with a small offset. The inset graph shows that at low current densities, the dependence can be roughly described by a logarithmic dependence on the current density, using the cell Tafel slope, which is determined in the next Section 3.3.

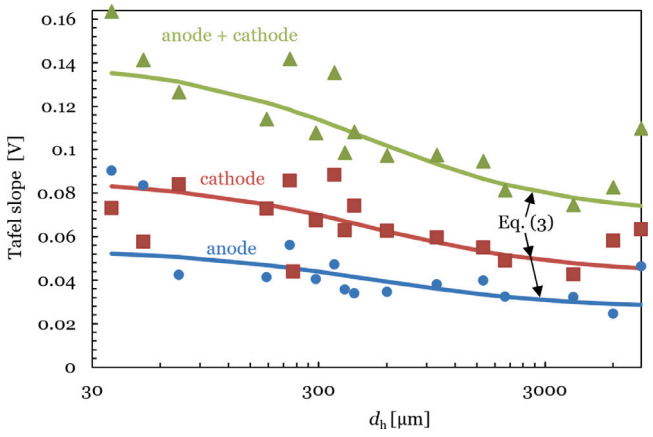

Fig. 6. Tafel slopes, on a natural logarithm basis, obtained from least-squares fits of the reference electrode measurements between $j = 10^2 - 10^3$ A/m^2 averaged over the three repetitions, without IR-correction. A few negative or almost zero values were discarded. The 232 μm sample showed anomalously low 0.04 V cathode and anomalously high 0.18 V anode Tafel slopes (outside graph range). The relatively high values for $d_h = 224$ and 353 μm may be related to the relatively high ohmic drop observed for these electrodes in Fig. 8, which tentatively could be attributed to reduced gas evacuation due to their diamond hole shape, as seen from their flat side, but without more data this is mostly speculation. The solid lines show the Tafel slope $\frac{2+d/d_c}{1+d/d_c}b$ of Eq. (4) with $d_c = 0.5$ mm, $b_a = 0.027$ V (62 mV/decade), and $b_c = 0.043$ V (100 mV/decade).

3.3. Tafel slopes

Because nickel oxidation seems to take place at lower current densities, we use the range $j = 10^2 - 10^3$ A/m^2. In a few instances, the reference electrodes clearly malfunctioned and yielded negative or almost zero Tafel slopes, which we discarded. Averaging the rest of the data over the three runs, the result is shown in Fig. 6.

Despite the large spread in the data, there seems to be a trend towards higher Tafel slopes for smaller holes. To explain this, we note that the inset of Fig. 5 shows that for current densities $10^2 \leq j \leq 10^3$ A/m^2 we can approximately write $\Delta V \approx b \ln\left(\frac{j}{J_{*t}}\right)$ with the Tafel slope $b = 0.07$ V (≈ 160 mV/decade) and $J_{*t} = 60$ A/m^2 the current density for which the transport losses ΔV approximately vanish. Adding this to the activation overpotential, the final term in Eq. (1) gives, after some

arithmetic, for $j \leq 10^3$ A/m^2:

$$b \ln\left(\frac{j}{J_*}\right) + \frac{\Delta V}{1 + d/d_c} \approx b_{\text{eff}} \ln\left(\frac{j}{J_{*\text{eff}}}\right), \tag{4}$$

where the effective exchange current density $J_{*\text{eff}} = J_*^{\frac{1+d/d_c}{2+d/d_c}} J_{*t}^{\frac{1}{2+d/d_c}}$ and an effective Tafel slope $b_{\text{eff}} = \frac{2+d/d_c}{1+d/d_c} b$ that for large holes $d \gg d_c$ gives a single Tafel slope b while for small hole sizes $d \ll d_c$ the Tafel slope tends to a doubled value $2b$.

Tafel slope doubling is a known and expected result from porous electrode theory in the case of ohmic limitations. This requires $j \gtrsim J_\kappa$, where the characteristic current density, with i = anode or cathode:

$$J_\kappa \equiv \frac{b_i \kappa}{l_{\text{el}}}. \tag{5}$$

The effective conductivity κ may be approximated by Eq. (3).

Even for zero gas fraction, the characteristic current density J_κ is below 10^3 A/m^2 for the smallest few electrodes, which have the smallest open area fraction, but almost an order of magnitude larger for the largest holes. Therefore, Tafel slope doubling is expected to occur for high current densities. However, using reference electrodes positioned at the back of the electrode, this doubling is only observable at much higher current densities than we used here, as we demonstrate in 2, this. Therefore, we are lead to the tentative conclusion that these additional losses η_{tr} occur outside the electrode holes, as is illustrated in Fig. 7.

The effective Tafel slope $\frac{2+d/d_c}{1+d/d_c} b$ of Eq. (4), is shown as solid lines in Fig. 6, and provides a reasonable fit of the trend.

For large holes, these fits tend to the values $2.3b_a = 62$ mV, $2.3b_c = 99$ mV, where $2.3 \approx \ln 10$ converts our values to the often used logarithm with base 10. These values are in good agreement with those reported in the literature for Tafel slopes of nickel under alkaline conditions for the oxygen evolution reaction (OER, typically 30–90 mV [55,56]) and hydrogen evolution reaction (HER, typically 100–120 mV [57,58]), respectively.

Interestingly, the largest holes and the smallest anode hole sizes seem to show a further increase in the Tafel slope 6, which may be the consequence of additional resistance that we did not correct for. Therefore, let us investigate and construct a theoretical model for these resistances.

3.4. Electrolyte resistance

The anodic and cathodic reference electrodes we used to determine the Tafel slopes in Fig. 6 were positioned behind the electrodes, schematically with the black filled circles in Fig. 7. The measured potential difference $\Delta\phi$ between the anolyte and catholyte may be thought of as consisting of a drop over the holes and over the diaphragm. For simplicity, we will assume here equal anode and cathode contributions. Averaging over the height of the electrode, the holes in the electrode may be treated as a porous medium. We will split the reactive surface area and, therefore, the exchange current density $J_* = J_{*\text{f}} + J_{*\text{h}} + J_{*\text{b}}$ and the current density $j = j_\text{f} + j_\text{h} + j_\text{b}$ into contributions from the diaphragm-facing front, the holes, and the back of the electrode, facing away from the diaphragm, respectively.

Equation (SI-5) gives an expression for the ohmic drop over the electrode holes, which combines with the ohmic drop over the diaphragm $\Delta\phi_\text{d} = l_\text{d}/\kappa_\text{d}$ and that over the holes $2\Delta\phi_\text{h} = 2j_\text{b} l_\text{e}/\kappa$ due to current reacting at the back to give for the total electrolyte potential drop $\Delta\phi = \Delta\phi_\text{d} + 2\Delta\phi_\text{h}$ to give

$$\Delta\phi = b \ln\left(1 + \frac{j}{2J_\text{c}}\right) + cj, \tag{6}$$

where $c = 2\frac{j_\text{b}}{j}\frac{l_\text{e}}{\kappa} + \frac{l_\text{d}}{\kappa_\text{d}}$ and the characteristic current density J_c will in general depend on current density. In case $j_\text{b} = 0$, Eq. (SI-4) gives $J_\text{c} \approx J_\kappa \frac{j/j_\text{h}}{1+j_\text{h}/6J_\kappa}$. For negligible ohmic losses, $j_\text{h} \ll J_\kappa$, the first term in Eq. (6) tends to the ohmic drop $j_\text{h} l_\text{e}/2\kappa$ over half the electrode thickness, expected in case the ionic current decreases linearly over the holes. For higher currents, the reaction inside the holes will preferentially take place close to the diaphragm, resulting in a smaller ohmic resistance, with an ohmic drop that is logarithmic in the current density. Ref. [28] reports on direct measurements of these *Galvani potential losses* using a reference electrode at the location of the diaphragm, which we did not use.

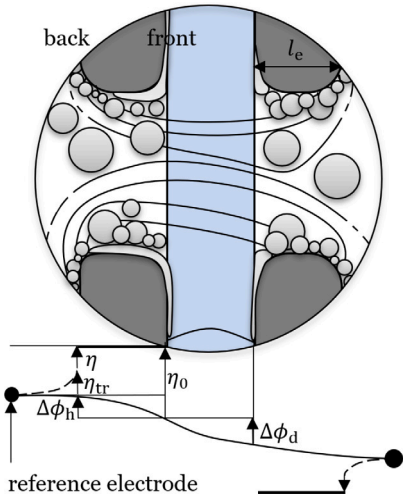

Fig. 7. A schematic of the diaphragm (light-blue), electrodes (dark grey), and gas (light grey). The solid line below the schematic illustrates the electrostatic potential along a particular current line traversing the bulk electrolyte behind the electrodes where the reference electrodes are also positioned (black circles) and then (dashed) to the electrodes. The difference with the electrode potentials (thick horizontal lines) is activation overpotential, η, and the difference between anode and cathode is the cell voltage minus the equilibrium voltage $V_{\text{cell}} - V_{eq} = 2\eta_0 + \Delta\phi_\text{d} = 2(\eta + \eta_{\text{tr}}) + \Delta\phi$ where $\eta_0 = \eta + \eta_{\text{tr}} + \Delta\phi_\text{h}$ is the front-side activation overpotential and $\Delta\phi = \Delta\phi_\text{d} + 2\Delta\phi_\text{h}$ the total Galvanic electrolyte potential drop, assuming equal anode and cathode losses.

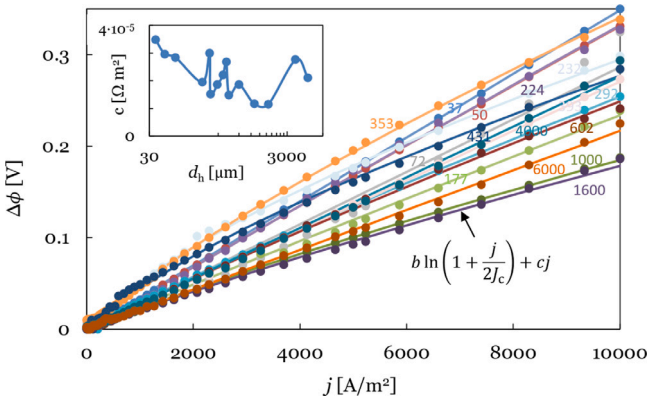

Fig. 8. The total Galvanic electrolyte potential drop $\Delta\phi = 2\Delta\phi_h + \Delta\phi_\text{d}$ over the holes and diaphragm measured between the reference electrodes positioned behind the anode and cathode, respectively. The solid lines give a fit of Eq. (6). The inset plot gives the fit values for the areal resistance c as a function of the hydraulic diameter d_h of the holes. Fig. 9 gives the fit result for the logarithmic term.

Instead, Fig. 8 shows the electrolyte potential drop between anolyte and catholyte reference, which we fitted with Eq. (6). The areal resistance is shown in an inset plot of Fig. 8 and shows a wide range of values between 0.35 Ω cm^2 for the smallest holes, a much lower value for intermediate-sized holes, and again higher resistances for the largest holes. While this agrees with, and therefore contributes to, the trend observed in the overall cell voltage of Fig. 4 it cannot account for the transport overpotential of Fig. 5, which was fitted with an even higher areal differential resistance of 0.76 Ω cm^2.

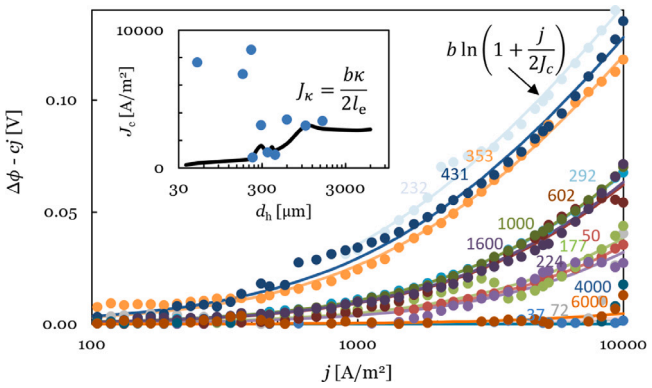

Fig. 9. The IR-corrected or logarithmic part of the electrolyte potential drop $\Delta\phi - cj \approx 2\Delta\phi_h$ measured between the anolyte and catholyte reference electrodes. The solid lines give a fit with the function $2\Delta\phi_h = b \ln\left(1 + \frac{j}{2J_c}\right)$ using $b = 0.07$ V (≈ 160 mV/decade), inspired by the porous electrode theory result of Eq. (6). The inset compares the fitted J_c with J_κ of Eqs. (3) and (5) with $b_l = b/2 = 0.035$ V and a constant gas fraction of $\varepsilon_g = 0.3$ and using the actual total electrode thickness l_{el} and open area fraction ϵ of each electrode. We find reasonable agreement for several electrodes with hole diameters $232 \le d_h \le 1600$ μm. With $J_c \approx (j/j_h)J_\kappa$, for $j_b = 0$, this suggests that, for these electrodes, most of the current reacts inside the holes. For three electrodes in this range $J_c \approx 2J_\kappa$, which could indicate that roughly half the current reacts inside the holes, or all at only at the anode or the cathode. Finally, for smaller and larger diameters (outside shown range) $J_c \gg J_\kappa$, implying that at most a very small fraction of the current reacts inside the holes.

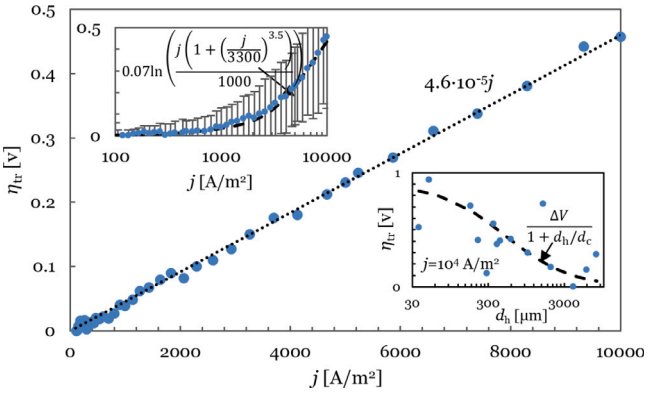

Fig. 10. Tafel plot of the summed anodic and cathodic transport activation overpotentials η_{tr}, obtained by subtracting the combined kinetic Tafel overpotential $0.07 \ln j$ from the reference electrode data, averaged over all hole sizes. The data can be described very well by an approximately constant resistance of 0.46 Ω cm². The top inset graph shows the same data in a Tafel plot, including bars that show the standard deviation in the data due to different hole sizes and the two runs. The $j = 10^4$ A/m² data point shows a small decrease, which is due to large scatter in the data for the few largest hole electrodes. The bottom inset shows the value for $j = 10^4$ A/m² as a function of hole hydraulic diameter along with the fit of the transport loss term in Eq. (2) using $\Delta V = 0.9$ V and $d_c = 0.5$ mm.

We note that the value $c \approx 0.115$ Ω cm² fit for the electrodes ZP100034 and ZP100890 with $d_h = 1$ and 1.6 mm is close to and even slightly below the expected membrane resistance of 0.13 Ω cm², which is never attained in zero-gap experiments [28,36].

Therefore, we can take this result to indicate that for these intermediate hole-size electrodes, the current distribution is very homogeneous, with most of the current lines taking the shortest possible route across the diaphragm. For the other electrodes, the ionic pathways are much larger and likely also include a significant part outside the diaphragm.

Fig. 9 shows the logarithmic part of Eq. (6), which fits the data very well. By Eq. (6), we attribute this to the potential drop over the electrode holes due to the fraction of the current reacting inside the holes. We note that it is significantly smaller in magnitude than the similar losses studied in Ref. [28]. Interestingly, it is most significant for intermediate hole-sized electrodes, with the largest and the smallest hardly showing any such logarithmic losses. What can explain this difference?

Comparing, for example, the electrodes with intermediate hole sizes $d_h = 1$ and 1.6 mm with those with the largest holes of 4 and 6 mm or those of the smallest holes of 37 and 72 μm, we see that the former have the lowest resistance and a clear logarithmic component, while the latter have a higher resistance and no distinguishable logarithmic component. The inset of Fig. 9 shows that intermediate holes have $J_c \approx J_\kappa$, while both small and large holes have $J_c \gg J_\kappa$.

Therefore, a possible explanation is that, while for intermediate-size holes most of the current reacts inside the holes ($j_h \approx j$), this is not the case for the very small and large holes ($j_h \ll j$). The higher areal resistance c that is observed in the inset of Fig. 8 is consistent with most of the current actually reacting at the back of the electrode ($j_b \approx j$). A largely inactive electrode front was also found in Ref. [20]. Therefore, we will next use imaging to have a look at what is going on at this front surface in Section 3.6. However, first, we further investigate the activation losses.

3.5. Activation overpotential

In Fig. 6, we already reported the Tafel slopes in the region $10^3 - 10^4$ A/m², measured using reference electrodes behind the electrodes. Here, we investigate these potentials up to 10^4 A/m², subtracting the expected Tafel overpotentials with slopes $b_a = 0.027$ V (62 mV/decade) and $b_c = 0.043$ (100 mV/decade). Fig. 10 shows the result upon averaging over all electrodes. Since the differences between the anode and cathode are small, we show their sum.

Surprisingly, we measure a very large additional voltage on top of Tafel kinetics. While it may be described in terms of a Tafel slope doubling at lower currents and roughly another doubling at current densities $j \gtrsim 3 \cdot 10^3$ A/m², a much simpler description is obtained in terms of an additional resistance of on average $4.6 \cdot 10^{-5}$ Ωm². This resistance is of the same order as the $7.6 \cdot 10^{-5}$ Ωm², associated with ΔV in Fig. 5 and may thus be at the origin of why small electrode holes give such high potential losses.

Fig. 10 shows the measured electrode potentials versus reference as a function of hydraulic hole diameter. With a few notable exceptions, these seem to follow very well the trend $\frac{0.9\ \text{V}}{1+d_h/0.5\ \text{mm}}$ that was also observed in the cell voltage of Fig. 4 showing again the likely origin of these losses.

Usually, compared to reference electrodes behind the electrodes, mostly kinetic overpotentials are measured, and only a small IR correction is needed. In our case, for the smallest holes, the IR component increases up to 1 V and is even larger than the activation losses. This is somewhat puzzling since, as illustrated in the schematic of Fig. 7, ohmic losses in the diaphragm and the holes of the electrodes would not be measured using our reference electrodes positioned behind the electrodes. Therefore, a significant potential drop has to be present between the location of the reference electrodes and the electrode. The simulations of Ref. [59] give about 60 mV difference in potential between the bulk electrolyte far away from the electrode and near the back of the electrode, so that a constant electrolyte resistance does not seem to be able to explain our much larger IR-losses.

A possible origin of this additional resistance may be a very dense bubble layer on the surface of the electrode, inside the holes and/or the back of the electrodes. Despite our much higher conductivity, the resistance that was found here is much larger than that found for bubble layers on free electrodes [38–40].

The resistance of $4.5 \cdot 10^{-5}$ Ωm² shown in Fig. 10 corresponds to an ohmic drop $l/\kappa_m \epsilon (1-\varepsilon)^{1.5}$ over a thickness $l = 1$ mm, with current restricted to an area fraction $\epsilon = 1/3$, using a gas fraction of $\varepsilon \approx 0.64$. So, such a resistance requires that the current traverses a very dense

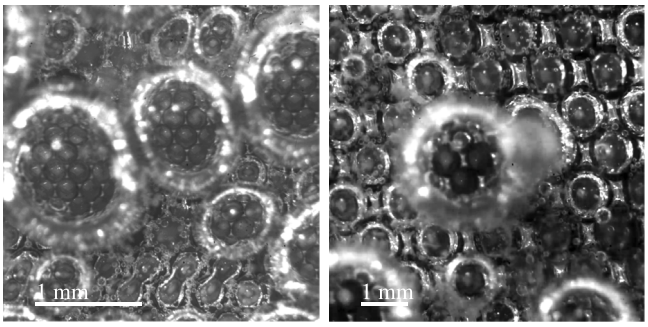

Fig. 11. Stills from high-speed video images of cathodes ZP200705 (d_h = 224 μm, left) and ZP200721 (d_h = 353 μm, right) for $j = 3.2 \cdot 10^3$ A/m^2 about 3 s after starting the current. Full videos are available as supplementary material here. Many hydrogen bubbles can be seen to cover one, two, or many holes.

bubble layer over a significant distance. Note that this value is close to the value used to make the final term of Eq. (2) comparable to the simulation result of Ref. [53].

Ref. [47] performed experiments at room temperature with a subset of the present electrodes and analysed the time behaviour after switching on a current. An additional resistance was found to arise over the time-scale of a few to many seconds, attributed to bubble accumulation, similar to Ref. [20]. The order of magnitude of this resistance, corrected for the lower conductivity, was in the range 0.1–1 Ω cm^2, similar to what we find here. Therefore, let us next investigate the gas distribution in more detail using imaging.

In the bottom inset graph of Fig. 10, the electrodes with d_h = 37 μm and d_h = 292 μm show less pronounced transport losses than the trend. They also showed a less pronounced logarithmic increase in an ohmic drop in Fig. 9 compared to some other relatively small hole electrodes, hinting at little reaction inside the holes. It is conceivable that in these cases, the primary reaction zone moved towards the front surface of the electrode. This avoids the large ohmic drops in reaching reactive areas all the way at the back of the electrode at the expense of a high ohmic resistance in the small bubble-filled gap between the electrode and the diaphragm. This gap resistance does not show up in the reference electrode data since it occurs outside this ionic pathway.

A possible hypothesis of what could cause the reaction to be forced to take place at the front of the electrodes is when the holes are completely blocked with gas. Let us, therefore, have a look at whether there is any direct evidence for the plausibility of this.

3.6. Imaging

First, we take a look at high-speed video images we made from the back of the electrodes, more or less in the centre of the electrode area. The movies of which Fig. 11 shows stills, show how hydrogen bubbles block many of the approximately 0.3 mm large holes. The same is found for oxygen and for wide ranges of current densities and hole sizes. We will quantify the behaviour in the next Section 3.7

Such blockage may have several deleterious effects. A direct effect is that the area of the holes covered with gas becomes unavailable, increasing activation overpotential. Indirectly, the gas has to be evacuated through a decreased area, likely leading to problems in evacuating gas from the narrow gap between the electrode front, increasing the gap resistance. Finally and rather speculatively, a reduced refreshment rate with the electrolyte behind the electrode could even lead to regions that are depleted of hydroxide ions since for $j \gtrsim 5 \cdot 10^3$ A/m^2 the limiting current density of the diaphragm [60,61] is exceeded.

To see what happens in the gap as a consequence of blocked holes, we made video images by looking through a transparent Nafion membrane. Such an approach was previously used in, e.g. Refs. [62–64]. While the contact angle of Nafion is similar to that of Zirfon [47], it is much less rigid and may, therefore, leave a larger gap than the Zirfon used in the experiments. Also, due to the imaging setup, the local current density at the viewing location may deviate from the average.

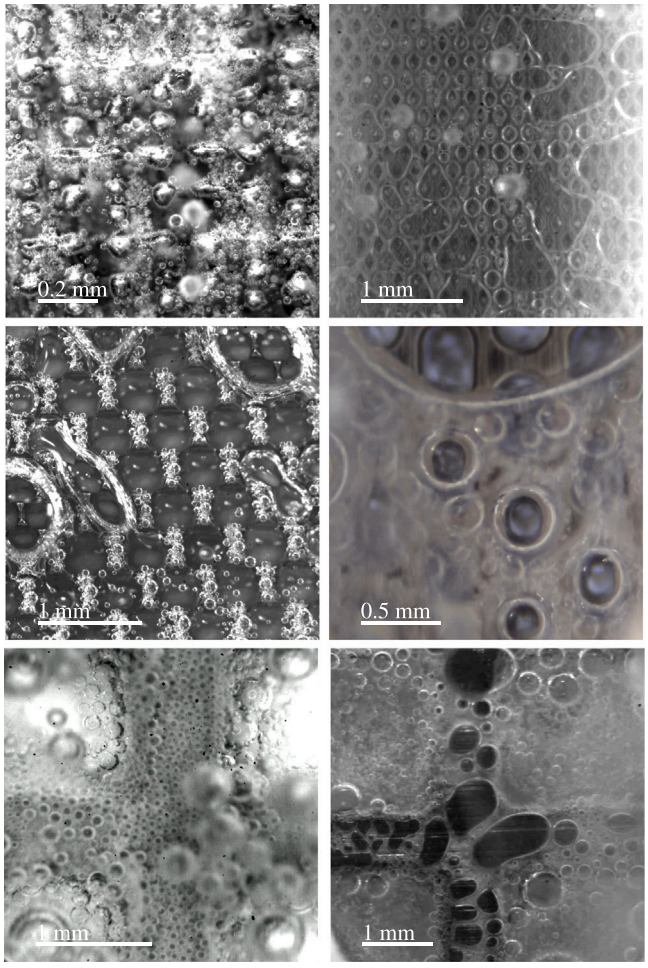

Fig. 12. Stills from videos (full versions, see SI) of cathodes ZP200728 (d_h = 72 μm, top), ZP200736 (d_h = 431 μm, middle), and the 2 mm squares for different current densities between $2 \cdot 10^3 < j < 5 \cdot 10^3$ A/m^2. On the left from the back, on the right, *through* a transparent membrane, 1–3 s after starting the current.

Fig. 12 shows the same electrode imaged both from the back (left) and the front (right) *through* of a transparent membrane. The small 72 μm holes shown at the top are virtually all blocked. Similar to in Ref. [63], we find that large gas slugs partly cover the gap between the electrode and diaphragm. A movie of the behaviour of this electrode in time at 10^4 A/m^2 for the anode provided in the supplementary material shows how part of the electrode seems inactive, emanating no bubbles, likely due to a large gas slug on the other side of the electrode facing the diaphragm.

For the d_h = 431 μm holes, shown in the middle of Fig. 12, these slugs transiently arise and disappear, creating a dynamic refreshment of electrolyte. Periods where many or most holes contain large single bubbles, both front and back, that completely block the holes, are alternated with periods of enhanced flow. For the still larger 2 mm holes shown in the bottom, the holes never fill completely with single bubbles.

These images thus largely confirm that gas in the gap between the diaphragm and the electrode can cause the current to be diverted to the holes or even the front of the electrode. To worsen this, smaller holes can fully clog with single bubbles. We will next investigate this further in the next section.

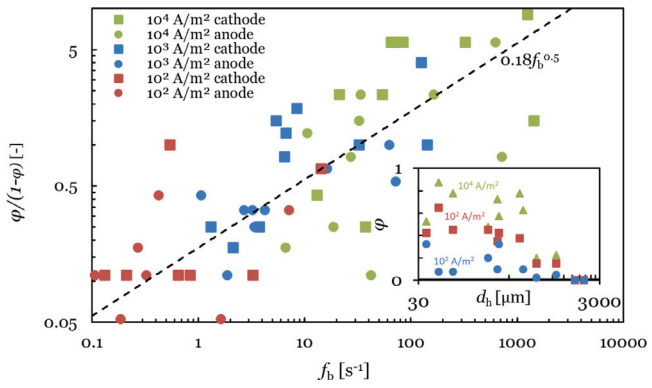

Fig. 13. The fraction of holes whose entrance is blocked by a single bubble, φ, divided by the fraction of unblocked holes $1-\varphi$, as a function of the frequency $f_b = 3U_g/2d_h$, introduced in Eq. (7), with which the volumetric gas flux $U_g = j\mathcal{V}_m/nF$ can generate a bubble of diameter equal to the hydraulic hole diameter d_h in each hole. A significant positive correlation is obtained over two decades of current density and a wide variety of electrodes for both the anode and the cathode.

3.7. Gas clogging

To improve our understanding of what influences the clogging observed in the previous section, we attempted to estimate the fraction φ of holes that are completely covered with bubbles for all imaged electrodes at three different current densities: 10^2, 10^3, and 10^4 A/m^2. The result is shown in the inset of Fig. 13. Unsurprisingly, smaller holes d_h and larger current densities j increase φ. There is a rather strong drop in φ for holes around $d \sim d_c = 0.5$ mm. To collapse all data to one master curve, we plot $\varphi/(1-\varphi)$ and find that it roughly scales with d_h/j to the power 0.46 for the cathode and 0.37 for the anode.

The volumetric gas flux $U_g = \frac{j\mathcal{V}_m}{nF}$ [m^3/s/m^2], with $n = 2$ for hydrogen and $n = 4$ for oxygen. The frequency f_b [s^{-1}] with this flux can generate in circular electrode holes of diameter d_h bubbles of equal diameter is given $f_b = \frac{\pi}{4}\pi d_h^2 U_g / \frac{\pi}{6} d_h^3 \epsilon = 3U_g/2d_h\epsilon$, so

$$f_b = \frac{3j\mathcal{V}_m}{2nFd_h\epsilon}. \tag{7}$$

In terms of this frequency, Fig. 13 shows a rough correlation

$$\varphi \sim \frac{1}{1+\sqrt{\frac{30\ \mathrm{s}^{-1}}{f_b}}}. \tag{8}$$

This relation implies that it takes roughly the volume of 30 bubbles of diameter equal to that of the hole to clog it, on average, half the time. Of course, bubbles are generated in various sizes, but through coalescence, they can grow to the size of the holes. Eq. (8) implies that the number of such large bubbles required to clog a hole is roughly independent of hole size or gas flux. A similar observation was made for the clogging of microchannel outlets by polystyrene balls [65]. While coalescence renders things more complicated, the universal nature of clogging behaviour from grain in silos, pedestrians near narrow doors, and objects floating in rivers [66], may be a useful guide to study clogging with bubbles in more detail.

3.8. Optimal hole size

The cell voltage shown in Fig. 4 suggests that neither very small nor very large holes lower the cell voltage. Therefore, a natural question is: What is the optimal hole size? Eq. (2) can be minimised with respect to d_h by setting the derivative of Eq. (2) with respect to d_h to zero, and solving for d_h, to give

$$d_{opt} \approx d_c\left(\sqrt{\frac{\Delta V}{fjd_c/\kappa_0}} - 1\right). \tag{9}$$

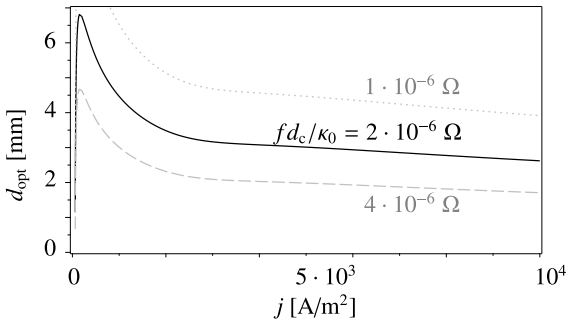

Fig. 14. The optimal hydraulic diameter d_{opt} of the holes in a zero-gap perforated-plate type electrode as a function of current density j. The lines give Eq. (9) using $d_c = 0.5$ mm with $fd_c/\kappa_d = 2\cdot10^{-6}$ Ω (black, solid), $4\cdot10^{-6}$ Ω (grey, dashed), and $1\cdot10^{-6}$ Ω (grey, dotted) and the fit shown in the inset of Fig. 5 to describe $\Delta V(j)$.

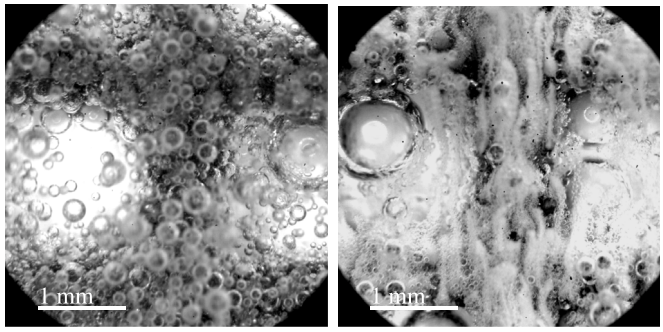

Fig. 15. The electrode ZP200719S ($d_h = 37$ μm) with 2 by 2 mm square holes cut out, 0.6 s (anode, left) and 0.3 s (cathode, right) after switching on the current density of 10^4 A/m^2. While at these times roughly the same amount of gas has been produced, large differences can be seen, as oxygen bubbles coalesce more to form larger bubbles [68], while hydrogen bubbles remain small and form plumes emanating from the smaller holes. (See supplementary material for full videos).

The larger the transport overpotential ΔV is compared to the current-distribution overpotential fjd_c/κ_d, the larger the optimal hole size. It also shows that if their ratio drops below 1, the optimal hole size tends to zero, which happens for low current densities in Fig. 14.

Fig. 14 plots Eq. (9) as a function of j, using the fits used in Figs. 4 and 5. Because the bubble transport losses ΔV do not decrease with decreasing current density as fast as the ohmic losses fjd_c/κ_d, the optimal hole size shows a peak at low current density. This is sensitive to the exact fit used for ΔV and completely disappears using the offset-linear fit of Fig. 5. Fig. 14 shows that over a wide range of high current densities, the optimum hardly depends on current density and is around $d_{opt} \approx 3$ mm.

In case of a fully active electrode, for example due to a small gap, the coefficient c may be substantially smaller, resulting in a smaller optimal hole size. On the other hand, for unaligned holes, the coefficient f may be substantially higher, resulting in a larger optimal hole size. To accommodate this variance, the grey lines in Fig. 14 indicate what happens in case of a halved or doubled value of f, compared to the value we used to fit our experiments.

In higher pressure electrolysers, the lower volumetric gas flux will likely decrease primarily ΔV, allowing smaller hole sizes to be optimal. For example, Ref. [67] found that decreasing the current density or increasing the pressure has a similar effect on the bubble layer resistance. However, to be sure how exactly the transport overpotentials ΔV will change at elevated pressures will require further research.

3.9. Combining large and small holes

Small holes and pillars can increase the reactive surface area compared to that of just the front and back of the electrode. However,

this advantage was overshadowed in our data by the disadvantage that small holes give in gas removal. This balance may be different at higher pressures, allowing smaller holes to be beneficial.

An idea to aid gas removal is to add, besides small holes, also larger perforations to induce flow in the gap and allow gas to escape more easily. In this way, we may combine the advantages of small holes with those of large holes. To try out this idea, we used the electrodes ZP200719S, which with $d_h = 37$ μm have the smallest holes of all tested electrodes. At 10^4 A/m^2, this had a cell voltage of 3.25, 3.11, and 3.31 V in runs 1, 2, and 3, respectively, averaging to 3.22 V. The inset plot in Fig. 13 shows that holes larger than 1 mm were never found to clog. Therefore, we cut out square holes of 2 mm by 2 mm, removing about 50 percent of the electrode area.

The measured cell voltage for these cut electrodes was measured to be 3.14 V, 0.08 V below the average of the three runs without these additional holes. So, despite a significant loss of about 50 percent in reactive surface area, these cut-out electrodes performed better in this one-off test. Fig. 15 shows the bubbles emanating from the small holes some time after switching on the current.

This result is only suggestive of the functioning of this idea, as we did not do enough experiments to statistically prove a sure improvement. More research may prove the viability and limits of such an approach.

4. Conclusions

Using a combination of electrochemical methods and imaging, a more or less consistent picture emerged of the influence of electrode shape on the current–voltage behaviour. We find that the most important parameter determining the cell voltage is the electrode hole size, which we parametrised in Fig. 4 in terms of the hydraulic diameter. Beyond a few millimetres, the cell voltage increases with increasing hole size, which we attributed to the ohmic drop that arises as the current distribution becomes more inhomogeneous. This was confirmed by measuring the electrolyte potential drop over the diaphragm, shown in the inset plot of Fig. 8.

A much stronger increase in cell voltage is associated with smaller holes than roughly a millimetre. Fig. 5 shows these losses are log-linear or offset-linear in the current density. For the smallest holes, they represent an additional resistance of $\sim 9 \cdot 10^{-5}$ Ωm^2, causing almost a Volt of additional overpotential at 10^4 A/m^2. The inset of Fig. 8 shows that about $\sim 2.5 \cdot 10^{-5}$ Ωm^2 of this additional resistance may be attributed to the electrolyte potential between bulk anolyte and catholyte. Figs. 8 and 9 seem to indicate that, while for intermediate hole size, a significant part of the reaction takes place in the electrode holes, in the smallest and largest holes, the reaction may for a large part take place primarily at the back of the electrode.

This agrees with the very large ohmic drop, on average $\sim 4 \cdot 10^{-5}$ Ωm^2 averaged over all electrodes, found between the electrodes and the reference electrodes positioned behind them in Fig. 10. Images taken from behind the electrodes show the dense bubble layers that may be responsible, as well as significant bubble clogging of small holes. Images taken from the front, *through* a transparent membrane, show how such hole clogging aggravates the formation of large gas slugs that inactivate large parts of the frontal area, forcing more of the reaction towards the back of the electrode.

We observed in Fig. 13 a reasonable rough correlation between the fraction of holes clogged and current density over the hole diameter, such that if about roughly 30 bubbles equal in diameter to the hole size are produced per second, this clogs about half the holes.

Eq. (9) gives that for atmospheric pressure, the optimal hole size of zero-gap electrodes lies in the millimetre range. However, great performance has been obtained with porous electrodes like felts or stacked meshes that have much smaller holes. The primary explanation may be sought in the wider pore size distribution present in such gas-diffusion electrodes, which allows for capillary action to remove gas. Alternatively, combining the positive features of small and large holes also holds substantial promise to deal with gas bubble losses effectively.

CRediT authorship contribution statement

J.W. Haverkort: Writing – original draft, Visualization, Validation, Supervision, Project administration, Methodology, Investigation, Funding acquisition, Formal analysis, Data curation, Conceptualization. **A.S. Aghdam:** Validation, Investigation, Data curation. **E.J.B. Craye:** Writing – review & editing, Validation, Investigation, Data curation.

Declaration of competing interest

The authors declare that they have no known competing financial interests or personal relationships that could have appeared to influence the work reported in this paper.

Acknowledgment

This publication is part of the projects “Better Electrodes for Water Electrolysis” (project number KICH1.ED04.20.011) and “Hydrogen bubbles quantified” (Vidi grant with project number 19665), (partly) financed by the Dutch Research Council (NWO). We thank W.L. van der Does for insightful feedback on our draft manuscript.

Appendix A. Supplementary data

Supplementary material related to this article can be found online at https://doi.org/10.1016/j.ijhydene.2025.150919.

References

[1] Sebbahi Seddiq, Assila Abdelmajid, Belghiti Amine Alaoui, Laasri Said, Kaya Savaş, Hlil El Kebir, et al. A comprehensive review of recent advances in alkaline water electrolysis for hydrogen production. Int J Hydrog Energy 2024;82:583–99.

[2] Jamesh Mohammed-Ibrahim, Hu Dingqin, Wang Jing, Naz Farah, Feng Jianpei, Yu Li, et al. Recent advances in noble metal-free electrocatalysts to achieve efficient alkaline water splitting. J Mater Chem A 2024.

[3] Kuhn AT, Bin Yusof J, Hogan P. The role of electrode structure and surface texture in the performance of gas evolving electrodes. J Appl Electrochem 1979;9:765–75.

[4] Brown Alan P, Krumpelt M, Loutfy RO, Yao NP. The effect of surface roughness on the hydrogen evolution reaction kinetics with mild steel and nickel cathodes. Electrochim Acta 1982;27(5):557–60.

[5] Ren Qiu, Feng Longsheng, Ye Congwang, Xue Xinzhe, Lin Dun, Eisenberg Samuel, et al. Nanocone-modified surface facilitates gas bubble detachment for high-rate alkaline water splitting. Adv Energy Mater 2023;13(39):2302073.

[6] Ma Jugang, Yang Mingye, Zhao Guanlei, Li Yangyang, Liu Biao, Dang Jian, et al. Ni electrodes with 3D-ordered surface structures for boosting bubble releasing toward high current density alkaline water splitting. Ultrason Sonochemistry 2023;96:106398.

[7] Li Mengxuan, Xie Pengpeng, Yu Linfeng, Luo Liang, Sun Xiaoming. Bubble engineering on micro-/nanostructured electrodes for water splitting. ACS Nano 2023;17(23):23299–316.

[8] Cheng Xu, Du Zhong-de, Ding Yu, Li Fu-yu, Hua Zhong-sheng, Liu Huan. Bubble management for electrolytic water splitting by surface engineering: A review. Langmuir 2023;39(48):16994–7008.

[9] Tourneur Jeoffrey, Joanny Loïc, Perrin Loïc, Paul Stéphane, Fabre Bruno. Efficient and highly stable 3D-printed NiFe and NiCo bifunctional electrodes for practical HER and OER. ACS Appl Eng Mater 2023;1(10):2676–84.

[10] Jiang Xinge, Kyriakou Vasileios, Song Chen, Wang Xianbin, Costil Sophie, Deng Chunming, et al. A novel multi-channel porous structure facilitating mass transport towards highly efficient alkaline water electrolysis. J Energy Chem 2024;93:511–8.

[11] Han Zhaojing, Zhao Hao, Peng Ci, Fan Chuanting, Wang Gang, Zhang Jie, et al. 3D-printed pyramid nickel-based electrode enabling directional bubble traffic and electrolyte flow for efficient hydrogen evolution. Int J Hydrog Energy 2024;64:476–86.

[12] Jin Liming, Cheng Zijun, Sun Tong, Gao Zijian, Deng Ling'ao, Yang Luyu, et al. Revealing the correlation between the hydrogen evolution reaction kinetics and multi-scale porous nickel electrode structure. J Power Sources 2025;646:237229.

[13] McCrory Charles CL, Jung Suho, Ferrer Ivonne M, Chatman Shawn M, Peters Jonas C, et al. Benchmarking hydrogen evolving reaction and oxygen evolving reaction electrocatalysts for solar water splitting devices. J Am Chem Soc 2015;137(13):4347–57.

[14] Lee Hae In, Cho Hyun-Seok, Kim MinJoong, Lee Jae Hun, Lee ChangSoo, Lee Sechan, et al. The structural effect of electrode mesh on hydrogen evolution reaction performance for alkaline water electrolysis. Front Chem 2021;9:787787.

[15] Li Long, Jiang Wenjun, Zhang Guang, Feng Deqiang, Zhang Ce, Yao Wei, et al. Efficient mesh interface engineering: insights from bubble dynamics in electrocatalysis. ACS Appl Mater Interfaces 2021;13(38):45346–54.

[16] Wei Xuesong, Umehara Yutaro, Nakajima Hironori, Ito Kohei, Etoh Atsuroh, Mori Shoji. Effect of mesh size of Ni wire mesh electrodes on alkaline water electrolysis performance: A study based on the observation of bubble departure behavior. Int J Hydrog Energy 2025;120:189–200.

[17] Jorne Jacob, Louvar Joseph F. Gas-diverting electrodes in the chlor-alkali membrane cell. J Electrochem Soc 1980;127(2):298.

[18] Kuhn M, Kreysa G. Modelling of gas-evolving electrolysis cells. III. The iR drop at gas-evolving electrodes. J Appl Electrochem 1989;19:720–8.

[19] Lafmejani Saeed Sadeghi, Müller Martin, Olesen Anders Christian, Kæ r Søren Knudsen. Experimental and numerical study of flow in expanded metal plate for water electrolysis applications. J Power Sources 2018;397:334–42.

[20] Haverkort JW, Rajaei H. Voltage losses in zero-gap alkaline water electrolysis. J Power Sources 2021;497:229864.

[21] Wu Rui, Hu Zhihao, Zhang Haojing, Wang Jinqing, Qin Chaozhong, Zhou Ye. Bubbles in porous electrodes for alkaline water electrolysis. Langmuir 2023;40(1):721–33.

[22] Liu Fulin, Wang Fangzhou, Hao Xiaowen, Fan Zhunfeng, Tan Jianyu. Effects of foam cathode electrode structure on alkaline water electrolysis for hydrogen production. Chem Eng Sci 2024;120307.

[23] Kou Tianyi, Wang Shanwen, Shi Rongpei, Zhang Tao, Chiovoloni Samuel, Lu Jennifer Q, et al. Periodic porous 3D electrodes mitigate gas bubble traffic during alkaline water electrolysis at high current densities. Adv Energy Mater 2020;10(46):2002955.

[24] Márquez Raúl A, Kawashima Kenta, Son Yoon Jun, Rose Roger, Smith Lettie A, Miller Nathaniel, et al. Tailoring 3D-printed electrodes for enhanced water splitting. ACS Appl Mater Interfaces 2022;14(37):42153–70.

[25] Tsuburaya Kensei, Obata Keisuke, Nagato Keisuke, Takanabe Kazuhiro. Porous substrate optimization for efficient water electrolysis: Uncovering electrocatalysts, electrolyte, and bubble dynamics effects. ACS Sustain Chem Eng 2024;12(44):16308–19.

[26] Kienzlen V, Haaf D, Schnurnberger W. Location of hydrogen gas evolution on perforated plate electrodes in zero gap cells. Int J Hydrog Energy 1994;19(9):729–32.

[27] Fischer Juergen, Hofmann Hans, Luft Gerhard, Wendt Hartmnt. Fundamental investigations and electrochemical engineering aspects concerning an advanced concept for alkaline water electrolysis. AIChE J 1980;26(5):794–802.

[28] Leuaa Pradipkumar, Kraglund Mikkel Rykær, Chatzichristodoulou Christodoulos. Decoupling of reaction overpotentials and ionic transport losses within 3D porous electrodes in zero-gap alkaline electrolysis cells. Electrochim Acta 2023;470:143306.

[29] Bleeker Jorrit, van Kasteren Celine, van Ommen J Ruud, Vermaas David A. Gas bubble removal from a zero-gap alkaline electrolyser with a pressure swing and why foam electrodes might not be suitable at high current densities. Int J Hydrog Energy 2024;57:1398–407.

[30] Sillen CWMP, Barendrecht E, Janssen LJJ, Van Stralen SJD. Gas bubble behaviour during water electrolysis. In: Hydrogen as an energy vector: proceedings of the international seminar, held in Brussels, 12–14 February 1980. Springer; 1980, p. 328–48.

[31] Kreysa G, Külps H-J. Experimental study of the gas bubble effects on the IR drop at inclined electrodes. J Electrochem Soc 1981;128(5):979.

[32] Kuhn M, Kreysa G. Modelling of gas-evolving electrolysis cells. II. Investigation of the flow field around gas-evolving electrodes. J Appl Electrochem 1989;19(5):677–82.

[33] Nishiki Yoshinori, Aoki Koichi, Tokuda Koichi, Matsuda Hiroaki. Primary current distribution in a two-dimensional model cell composed of an electrode with an open part. J Appl Electrochem 1984;14:653–61.

[34] Nishiki Y, Nakamatsu S, Aoki K, Tokuda K. Estimation of optimum anode geometry in chlor-alkali membrane cells. J Appl Electrochem 1989;19(1):90–4.

[35] Lanzi Oscar, Savinell Robert F, Horn Richard E. Some theoretical considerations on the design of a practical anode in an electrochemical reactor. J Appl Electrochem 1984;14(4):425–36.

[36] de Groot Matheus T, Vreman Albertus W. Ohmic resistance in zero gap alkaline electrolysis with a zirfon diaphragm. Electrochim Acta 2021;369:137684.

[37] Barros Rodrigo Lira Garcia, Scholl Jakob, Hoedemakers Inge, Liang Xiao Long, Skadell Karl, van der Schaaf John, et al. Impact of nickel electrode geometry on the electrochemical performance and bubble dynamics of a zero-gap alkaline electrolyzer. J Power Sources 2025;630:236116.

[38] Wang Bowen, Hao Minghui, Kirk Donald, Guay Daniel, Thorpe Steven. Analysis of bubble management performance using dual bubble layer model and electrochemical impedance spectroscopy. Electrochim Acta 2025;145784.

[39] Kitajima Daisuke, Misumi Ryuta, Kuroda Yoshiyuki, Mitsushima Shigenori. Relationship between bubble generation behavior and hydrogen evolution reaction performance at high current densities during alkaline water electrolysis. Electrochim Acta 2024;502:144772.

[40] Gomez M, Levitan D, Muñoz P, Falaguerra T, Longinotti MP, Humana T, et al. Unveiling OER bubble dynamics in alkaline electrolysis: Impacts on cell resistance. Int J Hydrog Energy 2025;106:138–45.

[41] Le Bideau Damien, Mandin Philippe, Benbouzid Mohamed, Kim Myeongsub, Sellier Mathieu. Review of necessary thermophysical properties and their sensivities with temperature and electrolyte mass fractions for alkaline water electrolysis multiphysics modelling. Int J Hydrog Energy 2019;44(10):4553–69.

[42] Khamene Sina Haghverdi, Creatore Mariadriana, Tsampas Mihalis N. 3D electrode surface engineering via atomic layer deposition of nickel oxide for improved water oxidation performance. Chem Eng J Adv 2025;22:100723.

[43] Albers Justin, Lau Marius, Bernaecker Christian Immanuel, Ashaju Abimbola, Harbiye Ahmad, Weissgaerber Thomas, et al. Highly active Raney-Nickel electrodes based on 3D pin structures for use in high temperature alkaline electrolysis. In: Electrochemical society meeting abstracts prime 2024. (42). The Electrochemical Society, Inc.; 2024, 2821–2821.

[44] Di Franco Francesco, Zaffora Andrea, Pupillo Davide, Seminara Barbara, Pärnamäe Ragne, Tedesco Michele, et al. Optimized base metals electrodeposition on Ni perforated plate type electrodes for high-performance alkaline water electrolysis. Int J Hydrog Energy 2024;70:548–56.

[45] Kurimoto Ryo, Tsubouchi Hiroki, Minagawa Hisato, Yasuda Takahiro. Pressure drop of gas–liquid taylor flow in square microchannels. Microfluid Nanofluidics 2020;24:1–15.

[46] Bhusan S, Ghosh Sumana, Das G, Das PK. Rise of taylor bubbles through narrow rectangular channels. Chem Eng J 2009;155(1–2):326–32.

[47] Craye EJB. Bubble quantification in the near electrode region in alkaline water electrolysis. Delft University of Technology; 2023.

[48] Vijverberg Lotte. Deactivation mechanisms and timescales of nickel electrodes in alkaline water electrolysis.

[49] Barros Rodrigo Lira Garcia, Kraakman Joost T, Sebregts Carlijn, van der Schaaf John, de Groot Matheus T. Impact of an electrode-diaphragm gap on diffusive hydrogen crossover in alkaline water electrolysis. Int J Hydrog Energy 2024;49:886–96.

[50] Gilliam Ryan J, Graydon JW, Kirk DW, Thorpe SJ. A review of specific conductivities of potassium hydroxide solutions for various concentrations and temperatures. Int J Hydrog Energy 2007;32(3):359–64.

[51] Haverkort JW. Electrolysers, fuel cells and batteries. TU Delft OPEN; 2024.

[52] Haverkort JW. A theoretical analysis of the optimal electrode thickness and porosity. Electrochim Acta 2019;295:846–60.

[53] Nishiki Yoshinori, Aoki Koichi, Tokuda Koichi, Matsuda Hiroaki. Current distribution in a two-dimensional narrow gap cell composed of a gas evolving electrode with an open part. J Appl Electrochem 1987;17:67–76.

[54] van der Does WL, Valle N, Haverkort JW. Multiphase alkaline water electrolysis simulations: The need for a solid pressure model to explain experimental bubble overpotentials. Int J Hydrog Energy 2025;102:295–303.

[55] Kibria MF, Mridha M Sh. Electrochemical studies of the nickel electrode for the oxygen evolution reaction. Int J Hydrog Energy 1996;21(3):179–82.

[56] Bocca C, Barbucci A, Cerisola G. The influence of surface finishing on the electrocatalytic properties of nickel for the oxygen evolution reaction (OER) in alkaline solution. Int J Hydrog Energy 1998;23(4):247–52.

[57] Krstajić Nedeljko, Popović Milica, Grgur Branimir, Vojnović Milan, Šepa Darko. On the kinetics of the hydrogen evolution reaction on nickel in alkaline solution: Part I. The mechanism. J Electroanal Chem 2001;512(1–2):16–26.

[58] Huot J-Y. Hydrogen evolution and interface phenomena on a nickel cathode in 30 w/o KOH: I. Kinetics parameters and electrode impedance between 303 and 363 K. J Electrochem Soc 1989;136(7):1933.

[59] Nishiki Yoshinori, Aoki Koichi, Tokuda Koichi, Matsuda Hiroaki. Secondary current distribution in a two-dimensional model cell composed of an electrode with an open part. J Appl Electrochem 1986;16:291–303.

[60] Haverkort JW, Rajaei H. Electro-osmotic flow and the limiting current in alkaline water electrolysis. J Power Sources Adv 2020;6:100034.

[61] Haverkort JW. Modeling and experiments of binary electrolytes in the presence of diffusion, migration, and electro-osmotic flow. Phys Rev Appl 2020;14(4):044047.

[62] Lentjes Dion. Effect of bubble behaviour on the performance of a zero-gap chlor-alkali electrolyzer. 2022.

[63] Qiu Huihang, Obata Keisuke, Tsuburaya Kensei, Nishimoto Takeshi, Nagato Keisuke, Takanabe Kazuhiro. Impact of gas bubble slug on high-frequency resistance and cell voltage in water electrolysis device. J Power Sources 2024;611:234765.

[64] Barros Rodrigo Lira Garcia, Kelleners Mathy HG, van Bemmel Lucas, van der Leegte Thijmen VN, van der Schaaf John, de Groot Matheus T. Elucidating the increased ohmic resistances in zero-gap alkaline water electrolysis. Electrochim Acta 2024;145161.

[65] Wyss Hans M, Blair Daniel L, Morris Jeffrey F, Stone Howard A, Weitz David A. Mechanism for clogging of microchannels. Phys Rev E—Statistical Nonlinear Soft Matter Phys 2006;74(6):061402.

[66] Marin Alvaro, Souzy Mathieu. Clogging of noncohesive suspension flows. Annu Rev Fluid Mech 2024;57.

[67] Janssen LJJ, Barendrecht E. Electrolytic resistance of solution layers at hydrogen and oxygen evolving electrodes in alkaline solution. Electrochim Acta 1983;28(3):341–6.

[68] Haverkort JW. A general mass transfer equation for gas-evolving electrodes. Int J Hydrog Energy 2024;74:283–96.